Journal of Catalysis 352 (2017) 274–281

Contents lists available at ScienceDirect

Journal of Catalysis

journal homepage: www.elsevier.com/locate/jcat

Two-channel photocatalytic production of H_2O_2 over g-C_3N_4 nanosheets modified with perylene imides

Liping Yang [a,b], Guohui Dong [a,*], Daniel L. Jacobs [c], Yuanhao Wang [a], Ling Zang [c,*], Chuanyi Wang [a,*]

[a] Laboratory of Environmental Science and Technology, Xinjiang Technical Institute of Physics and Chemistry, Key Laboratory of Functional Materials and Devices for Special Environments, Chinese Academy of Sciences, Urumqi 830011, People's Republic of China
[b] University of Chinese Academy of Sciences, Beijing 100049, People's Republic of China
[c] Nano Institute of Utah and Department of Materials Science and Engineering, University of Utah, Salt Lake City, UT 84112, USA

ARTICLE INFO

Article history:
Received 6 March 2017
Revised 16 May 2017
Accepted 17 May 2017
Available online 21 June 2017

Keywords:
Z-scheme
Hydrogen peroxide
Two-channel reaction
Perylene imide
g-C_3N_4

ABSTRACT

Hydrogen peroxide is a promising solar fuel and widely used in many industrial processes. Here we report on a new basis for clean energy storage, generating H_2O_2 from H_2O and O_2 by organic photocatalysis. In this study, we construct an all-solid-state Z-scheme heterojunction (PI_x-NCN) by assembling perylene imides (PI) on g-C_3N_4 nanosheets (NCN), where x is a percentage weight ratio of PI to NCN. PI_x-NCN exhibits significant enhancement in photocatalytic production H_2O_2, and the maximum enhancement was observed for $PI_{5.0}$-NCN. It was shown that PI can change H_2O_2 generation from single-channel to two-channel. Specifically, photoexcitation of the PI moieties transfers their conduction band electrons to the valence band of NCN, resulting in enhanced charge separation. Thus, more electrons are available to reduce O_2, producing more H_2O_2. More importantly, the holes in the valence band of PI moiety have more positive potential (2.08 V) than those of NCN (1.63 V), which can oxidize OH^- to form ·OH (1.99 V) and transform to H_2O_2 via the second channel. Therefore, for PI_x-NCN, the photogenerated electrons and holes can be separated into two different phases, helping spatially isolate the oxidation and reduction reaction sites, and thus minimizing the catalytic deactivation.

1. Introduction

Hydrogen peroxide (H_2O_2) is a promising high-energy product widely used in various fields [1–7], acting as both oxidant and reductant. In environmental remediation, H_2O_2 is an environmentally safe oxidant (its by-products are only H_2O and O_2) and is often used in wastewater treatment processes to remove organic impurities [1]. In the medical field, it can be used for disinfecting wounds and surgical tools [2]. More importantly than all of that, H_2O_2 can be used as a rocket fuel [3], as well as in fuel cells to generate electricity with water and oxygen as the byproduct [4–7]. Due to increasing energy demand, hydrogen peroxide has been proposed for a promising chemical fuel [6,7]. At present, many methods, including electrochemical synthesis [8], oxidation of alcohols, and anthraquinone autoxidation, have been adopted to produce H_2O_2 on a large scale [9,10]. However, these methods cannot be considered ideal approaches because they consume large amounts of energy and organic solvents. Moreover, organic impurities can contaminate the produced H_2O_2 and increase the difficulty of extraction [2]. To satisfy the demand for H_2O_2 and to eliminate the shortcomings of the conventional production methods, developing efficient, economical, and green technologies to produce H_2O_2 is critically important, for which the conversion of solar energy to chemical fuel becomes a fascinating approach.

Recently, researchers found that H_2O_2 can be produced through semiconductor photocatalytic processes. In these processes, H_2O_2 can be generated through photoreduction of O_2 in the presence of H_2O [11–13]. Since the involved driving force, sunlight, is abundant and renewable, semiconductor photocatalytic processes have attracted much attention. It was reported that TiO_2 and modified TiO_2 could function as effective photocatalysts for H_2O_2 production [14–16]. However, their photoresponse is limited to UV light due to their wide band gap, and UV light accounts for only 4% of the solar spectrum [17].

Recently, many researchers found that g-C_3N_4 could reduce O_2 to H_2O_2 under visible light [18–20]. For example, as reported in our previous work, H_2O_2 could be produced by g-C_3N_4 in the presence of carbon vacancies under visible light irradiation [18]. In addition, Shiraishi et al. reported that g-C_3N_4 can effectively produce H_2O_2 in a water/alcohol mixture under visible light irradiation [19,20]. Though g-C_3N_4 or modified g-C_3N_4 can produce H_2O_2 under visible light irradiation, the photogenerated holes in

* Corresponding authors. Fax: +86 0991 3838957 (C. Wang).
E-mail addresses: dongguohui@sust.edu.cn (G. Dong), lzang@eng.utah.edu (L. Zang), cywang@ms.xjb.ac.cn (C. Wang).

http://dx.doi.org/10.1016/j.jcat.2017.05.010
0021-9517/

these reported systems need to be captured by an organic scavenger (such as alcohol) to inhibit the recombination of photogenerated electrons and holes. Such scavengers may contaminate the produced H_2O_2, which reduces the advantages of using the photocatalytic approach for H_2O_2 production.

Rather than using a scavenger to consume the photogenerated holes, previous reports have shown that some photocatalysts are capable of oxidizing H_2O to O_2 or OH^- to ·OH with the photogenerated holes [21–23]. This suggests that H_2O might replace organic scavengers in inhibiting the recombination of photogenerated carries, thus preventing the H_2O_2 contamination. More importantly, ·OH may combine to form additional H_2O_2 [24], thus changing the H_2O_2 generation pathway from single-channel to two-channel. However, the photogenerated holes in g-C_3N_4 cannot oxidize OH^- to produce ·OH because the potential of the valence band of g-C_3N_4 is not positive enough [25,26]. As previously reported, the construction of Z-scheme heterojunctions can improve the oxidation ability of photogenerated holes [27–29]. In nature, the Z-scheme charge transfer process can separate photogenerated electrons and holes into two photosystems through an electron mediator [30]. Inspired by the advantages of photosynthesis and heterojunctions [31,32], we aimed to design an all-solid-state Z-scheme heterojunction photocatalyst based on g-C_3N_4 nanosheets, with which the photogenerated electrons and holes can be separated into two different phases, helping to spatially isolate the oxidation and reduction reaction sites, and thus minimize the catalytic deactivation.

Very recently, we constructed a Z-scheme heterojunction consisting of perylene imide (PI) molecules and g-C_3N_4 for nitric oxide (NO) removal under visible light [33]. PIs can be assembled on the edges of g-C_3N_4 through the reaction between perylene tetracarboxylic dianhydride (PTCDA) and the primary amine (—NH_2) edge groups on g-C_3N_4. Since the edges of g-C_3N_4 possess a limited amount of -NH_2, only a finite number of PI molecules can be assembled on the edges of g-C_3N_4. More importantly, the area of the g-C_3N_4 edge is very small; thus, the enhancement of photoactivity resulting from the heterojunction assembly is significantly limited. Consequently, it is reasonable to assume that g-C_3N_4 nanosheets (NCN) should possess a higher density of -NH_2 on the edges due to the increased ratio of edge to surface. As a result, more PIs may be assembled on the surfaces of g-C_3N_4 nanosheets, further improving the photocatalytic performance of g-C_3N_4.

In this study, an all-solid-state Z-scheme heterojunction photocatalyst has been successfully constructed by assembling PIs on ultrathin g-C_3N_4 nanosheets. It was found that the PTCDI-modified g-C_3N_4 nanosheets can change H_2O_2 generation from a single-channel pathway to a two-channel pathway, and thus significantly improve H_2O_2 generation. The structural information and photocatalytic H_2O_2 generation activity of different samples were investigated in detail.

2. Experimental

2.1. Catalyst preparation

2.1.1. Synthesis of g-C_3N_4 nanosheets (NCN)

g-C_3N_4 nanosheets (NCN) were prepared using a gas soft-template method. Typically, a mixture of melamine and cyanuric acid supplied by Adamas-beta (weight ratio 1:2) was placed in a crucible. Then this crucible was covered and calcined in a muffle furnace at 520 °C for 4 h with a heating rate of 20 °C/min. Following that, the resulted samples were ground and denoted as NCN.

2.1.2. Synthesis of PI_x-NCN

To prepare PI assembled nanosheeted g-C_3N_4 (PI_x-NCN; x represents the weight percentage of PTCDA, x = 2.5, 5, and 7.5), PTCDA was chosen to react with prepared NCN via the condensation reaction. First, PTCDA (appropriate amount), NCN (0.71 g), and imidazole (2.5 g) were placed in a 100 mL three-necked round-bottom flask with a reflux condenser. This mixture was then heated to 140 °C for 5 h under nitrogen. When the mixture was cooled to room temperature, 50 mL ethanol was added and stirred for another 12 h. Then the solution was poured into a 250 mL round-bottom flask containing 150 mL hydrochloric acid solution (2 mol/L). After being stirred for 12 h, the mixture was centrifuged and washed thoroughly with methanol and deionized water. The resulting red solid was transferred to a 100 mL round-bottom flask with 50 mL K_2CO_3 aqueous solution (10%) and heated at reflux in an oil bath at 100 °C for 1 h. After the solution cooled to 50 °C, it was centrifuged and washed three times with K_2CO_3 solution (10%), and then two times with HCl (2 mol/L), deionized water, and methanol, respectively. Finally, the collected solid were dried under vacuum at 80 °C for 12 h.

2.2. Characterization

The powder X-ray diffraction (XRD) patterns of all samples were measured on a Bruker D8 Advance diffractometer. X-ray photoelectron spectrometer (XPS) measurements were carried out on a VG Scientific ESCALAB MK II spectrometer equipped with two ultra-high-vacuum (UHV) chambers. UV–vis diffuse reflectance spectra (DRS) were recorded on a Solid Spec-3700 DUV spectrophotometer and were converted from reflection to absorption by the Kubelka–Munk method. Photoluminescence (PL) spectra were recorded on a fluorescence spectrophotometer (Hitachi, Model F-7000). Electron paramagnetic resonance (EPR) spectra were measured on a Bruker ElexsysE500 spectrometer.

2.3. Photocatalytic tests

Photocatalytic activity of different samples was evaluated through photocatalytic H_2O_2 generation. The visible light was obtained from a 300 W Xe lamp (CEL-HXF300) with a 420 nm cut-off filter. The incident light intensity was ca. 0.560 W/cm^2, measured by an optical power meter (Model 1916-C, Newport). The illumination area of the reaction vessel was 19.635 cm^2. Typically, 50 mg of specific samples (NCN or PI_x-NCN) was dispersed into 50 mL of distilled water in a container with an ice-water bath outside. Before light irradiation, the suspension was kept in the dark for 30 min to complete dark-controlled processes. Then visible light was turned on to start the photocatalytic reaction. During the photocatalytic reaction, about 2 mL of suspensions was taken from the glass container every 30 min for the detection of H_2O_2.

The concentration of H_2O_2 was detected by a fluorescence method according to our previous report [33]. Typically, the suspensions taken from the glass container were centrifuged to remove the photocatalysts. Then 50 μL of fluorescence reagent (described below) was added and reacted for 10 min. After that, 1 mL of 0.1 mol/L NaOH solution was added for the fluorescence measurements. The reaction product of H_2O_2 with the fluorescence reagent had a strong fluorescent emission at 409 nm.

To prepare the fluorescence reagent, 2.7 mg of p-hydroxyphenylacetic acid (POHPAA) and 1 mg of horseradish peroxidase were dissolved in a prepared potassium hydrogen phthalate buffer solution (10 mL, 8.2 g/L, pH 4.01) under stirring [34]. This reagent was stored in a refrigerator and refreshed every three days.

2.4. The stability of H_2O_2

To investigate if the generated H_2O_2 is stable on the surface of the resulting samples, a series of comparative experiments were carried out. The experiments were carried out in four similar glass

reactors with ice-water baths outside. Typically, 10 mg specific samples (NCN or $PI_{5.0}$-NCN) were dispersed into 50 mL of distilled water (A) or a certain concentration of hydrogen peroxide solution (the volume ratio of H_2O and H_2O_2 (30%) is 50:3; 0.057 mol/L) (B) under continuous stirring. Before light irradiation, the suspension was kept in the dark for 20 min for adsorption/desorption to reach equilibrium. Then 420 nm LED light was turned on to start the photocatalytic reaction. After irradiation for 90 min, about 2 mL of suspensions was taken from the reactor for H_2O_2 detection. If the H_2O_2 is stable on the surface of the sample, the differences in H_2O_2 concentration between A and B should be no less than 0.057 mol/L.

2.5. Electrochemical analysis

The photoelectrochemical measurements were carried out on an electrochemical workstation (CHI760C, Chenhua, China) with a conventional three-electrode cell. In the experiments, the prepared working electrode (described below) was positioned in the middle of a 0.1 M Na_2SO_4 aqueous solution with the glass side facing the incident light. When the photocurrent and cyclic voltammetry experiments were performed, a Xe lamp with 420 nm cutoff filter was chosen as the visible light source (0.560 W/cm^2). Meanwhile, a platinum plate (1.5 × 1.5 cm^2) and a saturated calomel electrode (SCE) were used as counter electrode and reference electrode, respectively. In Mott–Schottky experiments, the perturbation signal was 10 mV with frequency 100 Hz. Electrochemical impedance was carried out by sweeping the frequency from 100 kHz to 0.01 Hz with an AC amplitude of 5 mV at an ambient temperature. The Nyquist plot (Fig. S4b) is fitted using EC-lab software and interpreted as an equivalent circuit (inset) composed of solution resistance R_S, charge-transfer resistance R_{CT}, and constant phase element C_{DL}. The values of equivalent circuit elements are given in Table S1.

To prepare working electrodes, photocatalysts were dispersed in α-naphthol (0.5 wt.%) solution and were ground for 10 min. Subsequently, the resultant slurries were coated on a 1 × 1 cm fluorine tin oxide (FTO) glass substrate. Finally, this FTO glass was dried in air and annealed at 80 °C for 15 min [33].

2.6. EPR analysis

The spectra were recorded at the X band using a Bruker ElexsysE500 spectrometer with a 9.79 GHz magnetic field modulation at a microwave power level of 5.05 mW. In the experiments, 5,5-dimethyl-1-pyrroline N-oxide (DMPO) acts as a spin-trapping reagent. The measurements were carried out as follows: catalyst (2 mg) was suspended in 500 μL water or 500 μL chromatographic pure methanol containing 50 μL DMPO (the DMPO was prepared by adding 400 μL UP water into 40 μL commercial DMPO) to detect ·OH or $\cdot O_2^-$ within a Pyrex glass tube (capacity 1.5 mL), and the tube was sealed with a rubber septum cap. Following this, ultrasonication (10 min), the detection of $\cdot O_2^-$ in the air, and the detection of ·OH in an anaerobic environment with Ar bubbling (5 min) were carried out. Then the solution was photoirradiated (a 300 W Xe lamp with a 420 nm filter) with magnetic stirring for 3 min. After the irradiation, the resulting solution was subjected to analysis in a sealed capillary tube.

3. Results and discussion

The NCN was prepared by calcining a mixture of cyanuric acid and melamine at 520 °C for 4 h. PI_x-NCN (x [wt.%] = 2.5, 5.0, and 7.5) was prepared with PTCDA and NCN via a reflux condensation reaction (Scheme 1). As shown in Fig. 1a, the color of pure NCN is light yellow. However, after the condensation reaction, the color of PI_x-NCN samples changed to pink, correlating with the new broad absorption peak between 500 and 600 nm in diffuse reflectance UV–vis spectra (Fig. 1b). Based on these changes in prepared samples, we speculate that the PIs have assembled on g-C_3N_4 nanosheets. To probe this, fluorescence emission spectroscopy was used to study the fluorescence properties of resulted samples. As shown in Fig. 1c, the photoluminescence spectrum of PI_x-NCN exhibits a new emission peak at 571 nm corresponding to 0–1 singlet exciton transitions of PI molecules [35,36]. This further supports assembly of PIs on the surface of NCN. X-ray diffraction (XRD) (Fig. 1d) was used to monitor the phase structure of the resulting samples. PI_x-NCN shows two typical diffraction peaks at about 13.0° and 27.4°, respectively. The peak at 13.0° corresponds to the (100) crystal plane from the in-plane structural packing motif. The peak at 27.4°, corresponding to the (002) crystal plane, is characteristic of interlayer stacking. After the incorporation of PIs, the (002) peak was significantly strengthened due to enhanced face-to-face stacking of PI−PI or melem–PI units, indicating that the PI units may randomly assemble into the NCN framework and the obtained sheets have multiple layers. This inference can be proved by atomic force microscopy (AFM). As can be seen from Fig. S1 in the Supplementary Material, NCN shows the characteristics of ultrathin nanosheets with a thickness of about 12 nm (Figs. S1a and S1c). However, after the condensation reaction with PTCDA, the resulting PI_x-NCN sample was composed of a platelike structure with a thickness of about 140 nm (Figs. S1b and S1d), confirming that the ultrathin nanosheets were assembled layer by layer into a thick plate.

To further prove that PIs have assembled on the surface of PI_x-NCN, X-ray photoelectron spectroscopy (XPS) was employed to investigate the surface chemical composition of the prepared NCN and PI_x-NCN samples. As shown in survey spectra (Fig. 2a), carbon, nitrogen, and oxygen species can be detected in all samples. The high-resolution N1*s* spectrum of NCN can be deconvoluted into two peaks at binding energies of 398.5 and 400.8 eV (Fig. 2b). The peak at 398.5 eV is ascribed to sp^2-hybridized N atoms (C—N—C) in triazine rings, while the peak at 400.8 eV is assigned to the bridging N atoms (N—C_3) of the melem center [37]. Besides these two peaks, a new peak at 400.0 eV appears in the N1*s* spectrum of PI_x-NCN. This peak can be assigned to imide N atoms (O=C—N—C=O) [38], indicating that the reaction between PTCDA and the amino group has been achieved. In other words, PIs were assembled on the surface of PI_x-NCN. The high-resolution O1*s* spectrum (Fig. 2c) of NCN presents only one symmetrical weak peak at about 532.8 eV, which might come from adsorbed H_2O or surface hydroxyl groups [39]. For PI_x-NCN, this peak becomes stronger. Moreover, a new peak at 531.0 eV, which could be attributed to the C=O group [39], appears in the high-resolution XPS spectra of PI_x-NCN. The enhanced intensity and newly formed carbonyl group may come from imide groups of PIs, further confirming that PIs have assembled on the surface of NCN.

Photocatalytic activity of different samples was evaluated through photocatalytic H_2O_2 generation. Typically, 50 mg specific samples (NCN or PI_x-NCN) were dispersed into 50 mL distilled water in a container with an ice-water bath outside. Before light irradiation, the suspension was kept in the dark for 30 min to complete dark-controlled processes (e.g., adsorption balance). In this period, H_2O_2 cannot be detected in any sample systems. Then visible light was turned on to start the photocatalytic reaction. Fig. 3a shows that the concentration of H_2O_2 in all sample suspensions slowly increases with continued irradiation. In the same light irradiation time, more H_2O_2 is produced in PI_x-NCN suspension than in NCN suspension. After 120 min of irradiation, about 25, 60, 120, and 80 μmol of H_2O_2 were produced over NCN, $PI_{2.5}$-NCN, $PI_{5.0}$-NCN, and $PI_{7.5}$-NCN, respectively. According to the light intensity and concentration of generated H_2O_2, H_2O_2 quantum yield was cal-

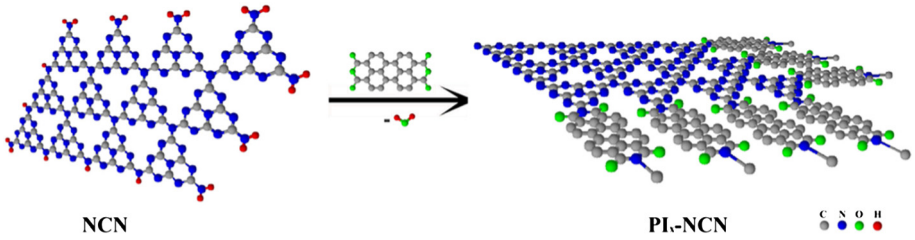

Scheme 1. Synthetic route of PI_x-NCN.

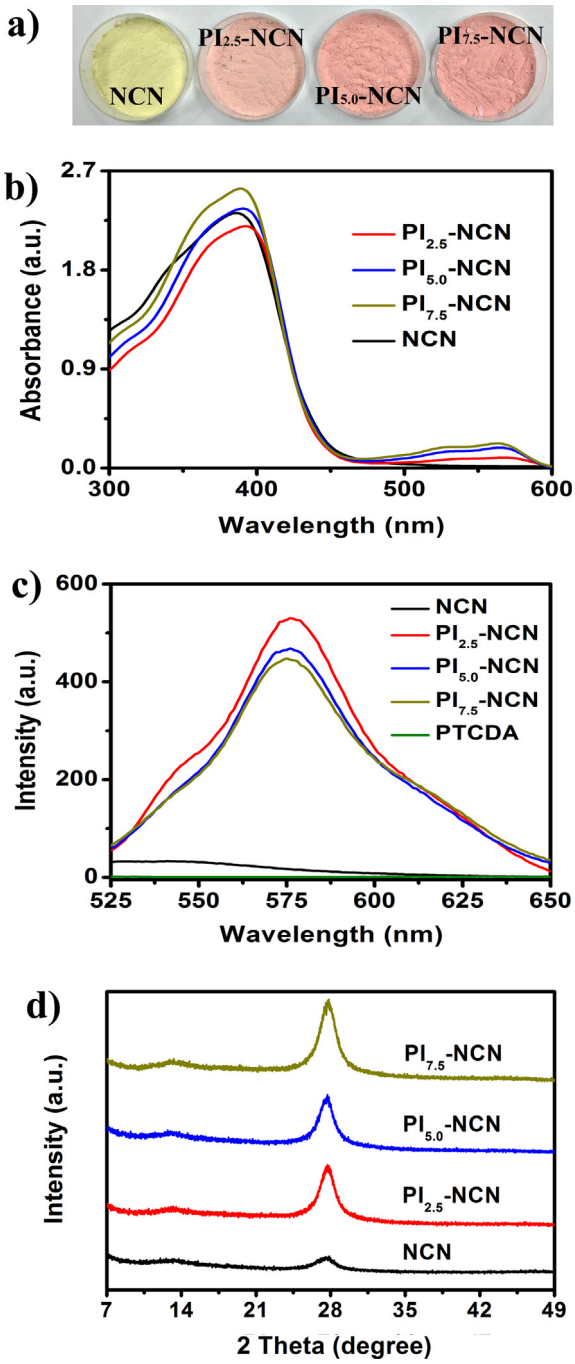

Fig. 1. (a) NCN (yellow) and PI_x-NCN (pink) solids showing different colors; (b) UV–vis diffuse reflection spectra of NCN and PI_x-NCN; (c) photoluminescent (PL) spectra of NCN and PI_x-NCN (excited at 500 nm); (d) XRD patterns of NCN and PI_x-NCN.

culated to be 0.8, 1.6, 3.2, and 1.8% min^{-1} for NCN, $PI_{2.5}$-NCN, $PI_{5.0}$-NCN, and $PI_{7.5}$-NCN, respectively (Fig. 3b). This clearly shows that the assembly of PIs can accelerate H_2O_2 generation of NCN by up to four times. However, excessive assembly of PI ($x > 5$) may inhibit the H_2O_2 generation, because excessive PI can hinder the light absorption ability of g-C_3N_4 nanosheets, as seen in the diffuse reflectance UV–vis spectra of samples in the range 300–450 nm (Fig. 1b).

According to previous reports, H_2O_2 could continue to be decomposed to H_2O and O_2 ($H_2O_2 \rightarrow H_2O + O_2$) [40]. Therefore, the stability of generated H_2O_2 on the surface of NCN and $PI_{5.0}$-NCN samples is investigated. A series of experiments were carried out in four similar glass reactors in an ice-water bath. Typically, 10 mg specific samples (NCN or $PI_{5.0}$-NCN) were dispersed into 50 mL distilled water (A) or 0.057 mol/L of H_2O_2 solution (B) under continuous stirring. A 420 nm LED lamp was chosen to start the photocatalytic reaction. After irradiation for 90 min, about 2 mL of the suspensions was taken from the reactor for H_2O_2 detection. If the H_2O_2 is stable on the surface of samples, the differences in H_2O_2 concentration between A and B should be no less than 0.057 mol/L. As shown in Fig. S2, the H_2O_2 solution does not decompose under visible light irradiation without the presence of photocatalysts. In a control experiment using NCN, the difference in H_2O_2 concentration is less than 0.057 mol/L, suggesting that the generated H_2O_2 on the surface of NCN is not stable. In contrast, the difference in H_2O_2 concentration in the $PI_{5.0}$-NCN system is more than 0.057 mol/L, which indicates that the generated H_2O_2 does not decompose on the surface of $PI_{5.0}$-NCN. The results suggest that the introduction of PIs inhibits H_2O_2 decomposition. Therefore, in the visible light irradiation process, the generated H_2O_2 in the $PI_{5.0}$-NCN system is more stable than that in the NCN system, indicating that PIs assembled on NCN are more suitable for photocatalytic H_2O_2 production.

Current understanding of the photocatalytic process includes three major steps: (1) photocatalysts are excited to produce electrons and holes; (2) generated electrons and holes migrate to the surface of photocatalyst; (3) surface electrons and holes trigger the redox reaction. The first step depends on the light absorption ability and band gap of the specific photocatalyst, which was monitored with UV–vis diffuse reflectance spectrometry (DRS). In contrast to NCN, all the PI_x-NCN samples display an additional absorption peak at about 500–600 nm (Fig. 1b). Combined with the fluorescence spectrum of samples excited at 500 nm (Fig. 1c), we can conclude that the additional absorption peak is due to the light absorption of PI in the PI_x-NCN system. The bandgap energy values of NCN and PI parts in the PI_x-NCN system were calculated to be 2.82 and 2.13 eV, respectively (Fig. S3). This result suggests that both NCN and PI parts in the PI_x-NCN system can be excited by visible light ($\lambda \geq 420$ nm). Therefore, a cooperative process involving both NCN and PI parts may occur in the photocatalytic process in the PI_x-NCN system.

After photoexcitation, the migration of generated charge carriers from the generation site to the photocatalyst surface is very important for the photocatalytic reaction. In general, generated

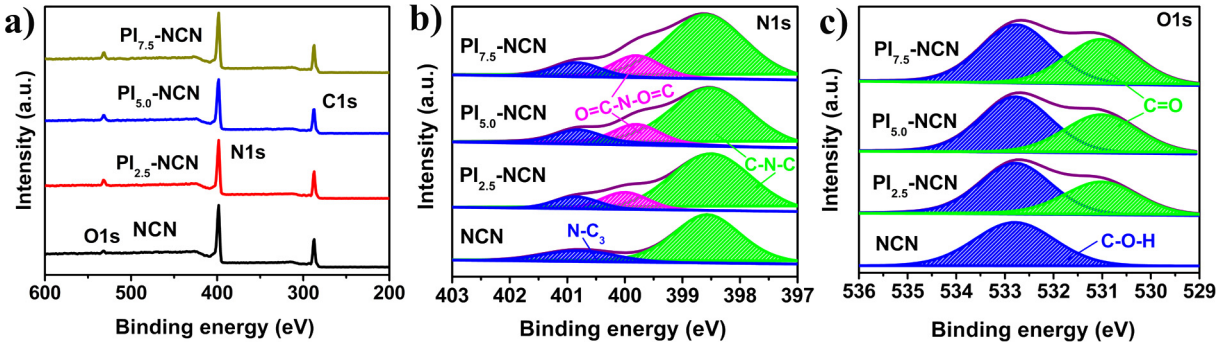

Fig. 2. (a) XPS spectra of NCN and PI_x-NCN. High-resolution XPS spectra of N1*s* (b) and O1*s* (c) of NCN and PI_x-NCN.

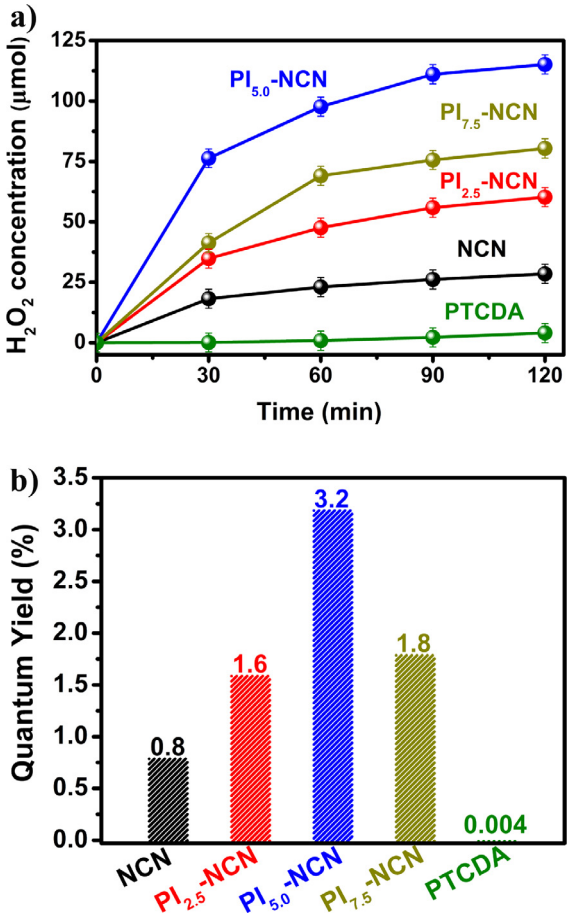

Fig. 3. (a) The concentrations of H_2O_2 generated in NCN and PI_x-NCN systems; (b) the calculated H_2O_2 quantum yields of NCN and PI_x-NCN.

carriers in NCN quickly recombine without a driving force for separation. Previous works revealed that the construction of heterojunctions can promote the separation of photogenerated carries [28,29,41]. We therefore speculated that the assembly of PI on the surface of NCN may favor the separation of photogenerated carries. To test this speculation, the transient photocurrent response of the photocatalysts was determined to explore the separation efficiency of photon-generated charge carriers. As shown in Fig. S4a, $PI_{5.0}$-NCN shows a 2× higher current density than NCN, which reveals that the mobility of the charge carriers is efficaciously elevated. Meanwhile, EIS measurements were carried out to investigate the interfacial charge transfer of different samples. Generally, a smaller semicircle arc of the EIS spectrum means a lower electron-transfer resistance value, signifying a faster interfacial charge transfer [44]. It can be seen from Fig. S4b that $PI_{5.0}$-NCN exhibits a smaller semicircular diameter than NCN, indicating that PIs can effectively improve the interfacial charge transfer of NCN.

When photogenerated electrons and holes arrive at the surfaces of semiconductors, their oxidation and reduction abilities are dependent on the valence band (VB) potential and conduction band (CB) potential, respectively. Therefore, Mott–Schottky plots were used to analyze the flat-band potential of different samples. As can be seen from Fig. 4a, both NCN and $PI_{5.0}$-NCN display n-type semiconductor characteristics. The flat-band potentials of NCN and $PI_{5.0}$-NCN were measured at −1.12 and −1.08 V vs. SHE, respectively. In n-type semiconductors, the flat-band potential is approximately at the CB potential [42]. Therefore, we conclude that the CB potentials of NCN and $PI_{5.0}$-NCN are −1.12 and −1.08 V. Since there is no significant difference between these two values, the measured CB potentials of $PI_{5.0}$-NCN may correspond to the CB position of the NCN part in the $PI_{5.0}$-NCN system. According to the formula for band gap (E_g = VB − CB), VB edge potentials were calculated to be 1.63 and 1.67 V for pure NCN and the NCN part in the $PI_{5.0}$-NCN system. To further determine the VB and CB positions of the PI part in the $PI_{5.0}$-NCN system, XPS valence band spectra of $PI_{5.0}$-NCN were measured. As shown in Fig. 4b, the edge of the valence band maximum energy for $PI_{5.0}$-NCN is 2.08 V. This value is more positive than that of NCN (1.63 V). We believe it is the VB position of the PI part in the $PI_{5.0}$-NCN system. Based on the formula for the band gap, the CB edge potential of the PI part in the $PI_{5.0}$-NCN system was calculated to be 0.05 V. Based on these data, the band structure diagram of the $PI_{5.0}$-NCN system is proposed as shown in Fig. 4c.

Based on analysis of the charge separation model in the PI_x-NCN system (a detailed explanation can be found in the Supplementary Material), we conclude that the migration of electrons between the PI part and the NCN part is from the CB of PI to the VB of NCN, suggesting that the charge separation model in the PI_x-NCN system is Z-scheme charge migration. In a Z-scheme model, the photogenerated electrons in the CB of NCN trigger the reduction reaction. Although the reduction potential of H_2O/H_2 (0 V vs. SHE) is more positive than that of $O_2/{}^{\cdot}O_2^-$ (−0.33 V vs. SHE), the large hydrogen overpotential makes hydrogen evolution more difficult than oxygen activation. Therefore, the photogenerated electrons are preferentially used to reduce O_2 to ${}^{\cdot}O_2^-$. Since there is no significant difference in CB potential between NCN and $PI_{5.0}$-NCN, both NCN and $PI_{5.0}$-NCN could reduce O_2 to ${}^{\cdot}O_2^-$. Despite this, $PI_{5.0}$-NCN would produce more ${}^{\cdot}O_2^-$ than NCN because $PI_{5.0}$-NCN possesses more effective electrons. To probe this, the DMPO spin-trapping ESR technique in combination with the nitroblue tetrazolium (NBT) degradation method was employed to measure the production of ${}^{\cdot}O_2^-$ in photocatalysis. As shown in Fig. 5a, the characteristic peaks of DMPO-${}^{\cdot}O_2^-$ can be observed in both NCN and $PI_{5.0}$-NCN systems.

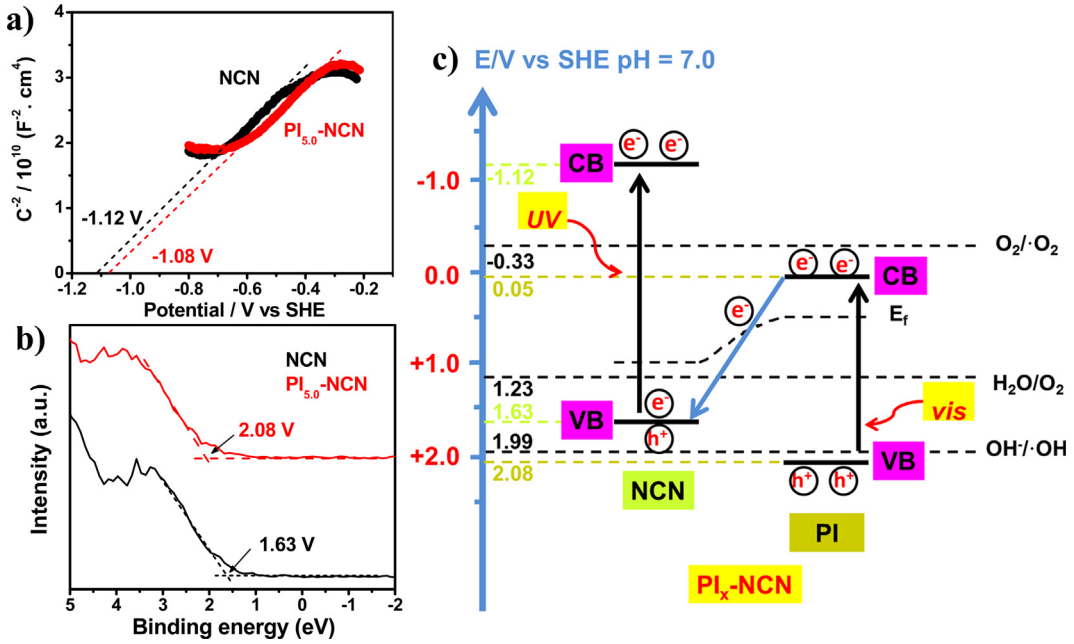

Fig. 4. (a) Mott–Schottky plot of NCN and $PI_{5.0}$-NCN at 100 Hz obtained in the dark; (b) VBXPS of NCN and $PI_{5.0}$-NCN; and (c) band structures of NCN and PI_x-NCN.

However, the ESR signals of DMPO-$\cdot O_2^-$ observed in the $PI_{5.0}$-NCN system are much stronger than that observed in the NCN system. Meanwhile, the degradation of nitroblue tetrazolium (NBT) was employed to compare the amount of $\cdot O_2^-$ generated from different suspensions (Fig. S5). After 2 h, the degradation degree of NBT in NCN and $PI_{5.0}$-NCN systems is 18.5 and 28.4%, respectively, suggesting that $PI_{5.0}$-NCN could generate more $\cdot O_2^-$. Our previous work revealed that $\cdot O_2^-$ can be further reduced to H_2O_2 [43]. Therefore, $PI_{5.0}$-NCN could produce more H_2O_2 than NCN through the reduction reaction, which is triggered by the photogenerated electrons.

Besides the reduction reaction, the oxidation reaction can be triggered by the photogenerated holes, which are in the VB of the PI part. The VB potential of the PI part was tested to be 2.08 V, while the reduction potential of $OH^-/\cdot OH$ is 1.99 V [43]. The more positive VB potential of the PI part than the reduction potential of $OH^-/\cdot OH$ suggests that $PI_{5.0}$-NCN could oxidize OH^- to $\cdot OH$ under visible light thermodynamically. In contrast, NCN could not oxidize OH^- to $\cdot OH$ under the same conditions because the VB potential of pure NCN is more negative than the reduction potential of $OH^-/\cdot OH$. To further prove this point, the DMPO spin-trapping ESR technique was employed to identify the production of $\cdot OH$ under anaerobic conditions. As shown in Fig. 5b, the characteristic peaks of DMPO-$\cdot OH$ cannot be observed in the NCN system. However, obvious DMPO-$\cdot OH$ signals can be observed in the $PI_{5.0}$-NCN system, confirming that holes generated from the excitation of $PI_{5.0}$-NCN could oxidize surface adsorbed OH^- or H_2O to produce $\cdot OH$. Since $\cdot OH$ can transform to H_2O_2 through combination with each other, $PI_{5.0}$-NCN could produce H_2O_2 through the oxidation reaction triggered by the photogenerated holes, which could not occur in the NCN system. Therefore, the assemblies of PI can change the H_2O_2 generation from a single-channel pathway to a two-channel pathway.

To further clarify the generation mechanism of H_2O_2 over NCN and $PI_{5.0}$-NCN, a series of active species trapping experiments were carried out (Figs. 6 and S6). First, we studied the role of O_2 in H_2O_2 generation over NCN and $PI_{5.0}$-NCN by bubbling high-purity nitrogen to eliminate O_2 in the photocatalysis process. It was found that the H_2O_2 generation on both NCN and $PI_{5.0}$-NCN was not completely depressed, suggesting that dissolved oxygen is not the only source of H_2O_2, which can also be proved by the hole-trapping experiments. This is not surprising, because both NCN and $PI_{5.0}$-NCN can oxidize H_2O to O_2. Moreover, in both the O_2 elimination

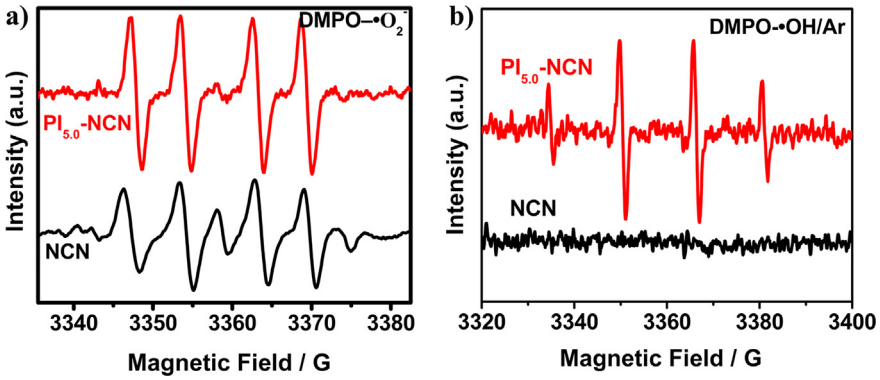

Fig. 5. (a) DMPO spin-trapping ESR spectra recorded for $\cdot O_2^-$ in the NCN and $PI_{5.0}$-NCN systems (under $\lambda > 420$ nm irradiation); (b) DMPO spin-trapping ESR spectra recorded for $\cdot OH$ in the NCN and $PI_{5.0}$-NCN systems under anaerobic condition (under $\lambda > 420$ nm irradiation).

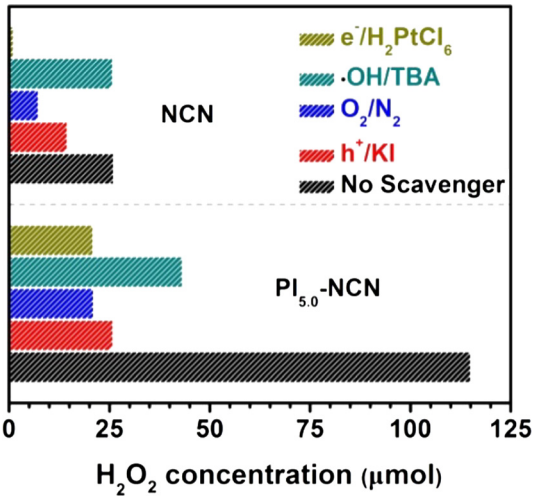

Fig. 6. The influence of scavengers (H_2PtCl_6, KI, TBA, N_2 for e^-, h^+, ·OH, O_2, respectively) on photocatalytic H_2O_2 production using NCN and $PI_{5.0}$-NCN. The photocatalytic conditions are the same as in Fig. 3a.

experiment and the hole-trapping experiment, the depression effects for H_2O_2 generation on NCN are not as serious as those on $PI_{5.0}$-NCN. One reason is that PI assembly can produce more O_2; the other reason may relate to ·OH, which can transform to H_2O_2 through combination with each other. Therefore, chloroplatinic acid (H_2PtCl_6) and *tert*-butyl alcohol (TBA) was used to eliminate e^- and ·OH, respectively, to verify our speculation. As seen for NCN with H_2PtCl_6, H_2O_2 generation was scarcely observed, but $PI_{5.0}$-NCN still exhibited H_2O_2 generation, indicating that $PI_{5.0}$-NCN has an alternative source for H_2O_2 generation. Meanwhile, the addition of TBA clearly depressed the H_2O_2 generation of $PI_{5.0}$-NCN, but not NCN, which further shows that H_2O_2 in the $PI_{5.0}$-NCN system has a second source (·OH), and the attenuation amount belongs to the additional H_2O_2 generated from ·OH for $PI_{5.0}$-NCN, which is about three times the H_2O_2 amount for pure NCN. Thus, this confirms that the assemblies of PI can change the H_2O_2 generation from single-channel to two-channel, and we can summarize that the second pathway for $PI_{5.0}$-NCN greatly promotes H_2O_2 generation from NCN via single-channel.

Based on these observations, the photocatalytic generation of H_2O_2 over $PI_{5.0}$-NCN involves the following six reactions:

$$PI_{5.0}\text{-NCN} + \text{visible light} \rightarrow h^+ + e^-, \quad (1)$$

$$2h^+ + H_2O \rightarrow O_2 + 2H^+, \quad (2)$$

$$h^+ + OH^- \rightarrow \cdot OH, \quad (3)$$

$$\cdot OH + \cdot OH \rightarrow H_2O_2, \quad (4)$$

$$e^- + O_2 \rightarrow \cdot O_2^-, \quad (5)$$

$$e^- + \cdot O_2^- + 2H^+ \rightarrow H_2O_2. \quad (6)$$

In comparison, the photocatalytic generation of H_2O_2 over NCN only involves four reactions:

$$NCN + \text{visible light} \rightarrow h^+ + e^-, \quad (7)$$

$$2h^+ + H_2O \rightarrow O_2 + 2H^+, \quad (8)$$

$$e^- + O_2 \rightarrow \cdot O_2^-, \quad (9)$$

$$e^- + \cdot O_2^- + 2H^+ \rightarrow H_2O_2. \quad (10)$$

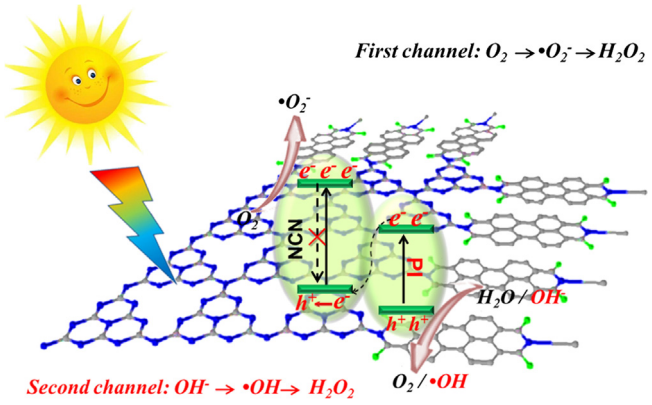

Fig. 7. Schematic illustration of producing H_2O_2 via a two-channel pathway at different sites on all-solid-state Z-scheme heterojunctions.

To check the stability of PI_x-NCN during photocatalytic H_2O_2 generation, the recycling test of $PI_{5.0}$-NCN and the structure analysis of used $PI_{5.0}$-NCN were explored. Interestingly, the photocatalytic H_2O_2 generation activity of $PI_{5.0}$-NCN did not significantly decline after 10 cycles (Fig. S7a), suggesting that the performance of $PI_{5.0}$-NCN is very stable during photocatalytic H_2O_2 production. Moreover, no significant changes can be found in the color (Fig. S7b), XRD (Fig. S8a), XPS (Fig. S8d), UV–vis diffuse reflection spectra (Fig. S8b), or photoluminescence emission peak (at about 571 nm, Fig. S8c) after 10 cycles, indicating that the structure of $PI_{5.0}$-NCN is very stable during photocatalytic H_2O_2 production.

4. Conclusions

In summary, an all-solid-state Z-scheme heterojunction photocatalyst has been successfully constructed by assembling PI on ultrathin g-C_3N_4 nanosheets. Interestingly, the assemblies of PI can change the H_2O_2 generation pathway from a single-channel pathway to a two-channel pathway, and thus can significantly improve the H_2O_2 generation performance of NCN, as shown in Fig. 7, a schematic illustration of producing H_2O_2 via a two-channel pathway at different sites on an all-solid-state Z-scheme heterojunction. The results of photoluminescence spectra and band structure analysis show that the prepared PI_x-NCN is a Z-scheme heterojunction, which improves the charge separation efficiency. Therefore, more electrons from the CB of the NCN part can reduce O_2 to produce more H_2O_2. Additionally, the holes in the VB of the PI part can trigger the oxidation reaction. Because the VB potential of PI is more positive than that of NCN, the holes of PI_x-NCN can oxidize OH^- to ·OH, which can subsequently react to produce H_2O_2. This study not only provides a new strategy for improving photocatalytic H_2O_2 production, but also provides new insight into the design of effective photocatalysts.

Acknowledgments

Financial support by the National Nature Science Foundation of China (Grants 21473248 and 21603271), the CAS-SAFEA International Partnership Program for Creative Research Teams, and the NSF (CBET 1502433) is gratefully appreciated.

Appendix A. Supplementary material

Supplementary data associated with this article can be found, in the online version, at http://dx.doi.org/10.1016/j.jcat.2017.05.010.

References

[1] J.M. Campos-Martin, G. Blanco-Brieva, J.L. Fierro, Angew. Chem. Int. Ed. 45 (2006) 6962–6984.
[2] I.H. Kim, H. Tanaka, T. Iwasaki, T. Takubo, T. Morioka, Y. Kato, Water Sci. Technol. 57 (2008) 195–200.
[3] E. Wernimont, M. Ventura, G. Garboden, P. Mullens, General Kinetics, LLC, Aliso Viejo, CA, 1999.
[4] S. Fukuzumi, Y. Yamada, K.D. Karlin, Electrochim. Acta 82 (2012) 493–511.
[5] Y. Yamada, M. Yoneda, S. Fukuzumi, Energy Environ. Sci. 8 (2015) 1698–1701.
[6] M. Jakešová, D.H. Apaydin, M. Sytnyk, K. Oppelt, W. Heiss, N.S. Sariciftci, E.D. Głowacki, Adv. Func. Mater. 26 (2016) 5248–5254.
[7] K. Mase, M. Yoneda, Y. Yamada, S. Fukuzumi, Nat. Commun. 7 (2016).
[8] L.V. Pham, J. Messinger, Biochem. Biophys. Acta. 1837 (2014) 1411–1416.
[9] T. Iwahama, S. Sakaguchi, Y. Ishii, Org. Process Res. Dev. 4 (2000) 94–97.
[10] V.R. Choudhary, A.G. Gaikwad, S.D. Sansare, Angew. Chem. Int. Ed. 40 (2001) 1776–1779.
[11] S. Kato, J. Jung, T. Suenobu, S. Fukuzumi, Energy Environ. Sci. 6 (2013) 3756.
[12] N. Kaynan, B. Berke, O. Hazut, R. Yerushalmi, J. Mater. Chem. A 2 (13) (2014) 822.
[13] Y. Yamada, A. Nomura, T. Miyahigashi, S. Fukuzumi, Chem. Commun. 48 (2012) 8329–8331.
[14] R. Cai, Y. Kubota, A. Fujishima, J. Catal. 219 (2003) 214–218.
[15] G. Moon, W. Kim, A.D. Bokare, N. Sung, W. Choi, Energy Environ. Sci. 7 (2014) 4023–4028.
[16] M. Teranishi, S.I. Naya, H. Tada, J. Am. Chem. Soc. 132 (2010) 7850–7851.
[17] D. Wang, T. Kako, J. Ye, J. Am. Chem. Soc. 130 (2008) 2724–2725.
[18] S. Li, G. Dong, R. Hailili, L. Yang, Y. Li, F. Wang, Y. Zeng, C. Wang, Appl. Catal. B Environ. 190 (2016) 26–35.
[19] Y. Shiraishi, S. Kanazawa, Y. Sugano, D. Tsukamoto, H. Sakamoto, S. Ichikawa, T. Hirai, ACS Catal. 4 (2014) 774–780.
[20] Y. Shiraishi, Y. Kofuji, H. Sakamoto, S. Tanaka, S. Ichikawa, T. Hirai, ACS Catal. 5 (2015) 3058–3066.
[21] A. Ishikawa, T. Takata, J.N. Kondo, M. Hara, H. Kobayashi, K. Domen, J. Am. Chem. Soc. 124 (2002) 13547–13553.
[22] F. Meng, J. Li, S.K. Cushing, J. Bright, M. Zhi, J.D. Rowley, Z. Hong, A. Manivannan, A.D. Bristow, N. Wu, ACS Catal. 3 (2013) 746–751.
[23] J. Zhang, Y. Nosaka, J. Phys. Chem. C 118 (2014) 10824–10832.
[24] F. Freund, V. Stolc, Animals 3 (2013) 513–531.
[25] X. Wang, K. Maeda, A. Thomas, K. Takanabe, G. Xin, J.M. Carlsson, M. Antonietti, Nat. Mater. 8 (2009) 76–80.
[26] T. Xiong, W. Cen, Y. Zhang, F. Dong, ACS Catal. 6 (2016) 2462–2472.
[27] T. Hisatomi, J. Kubota, K. Domen, Chem. Soc. Rev. 43 (2014) 7520–7535.
[28] A. Kudo, Y. Miseki, Chem. Soc. Rev. 38 (2009) 253–278.
[29] H. Wang, L. Zhang, Z. Chen, J. Hu, S. Li, Z. Wang, J. Liu, X. Wang, Chem. Soc. Rev. 43 (2014) 5234–5244.
[30] P. Zhou, J.G. Yu, M. Jaroniec, Adv. Mater. 26 (2014) 4920–4935.
[31] H. Li, Y. Zhou, W. Tu, J. Ye, Z. Zou, Adv. Func. Mater. 25 (2015) 998–1013.
[32] G. Liu, G. Zhao, W. Zhou, Y. Liu, H. Pang, H. Zhang, D. Hao, X.G. Meng, P. Li, T. Kako, J. Ye, Adv. Func. Mater. 26 (2016) 6822–6829.
[33] G. Dong, L. Yang, F. Wang, L. Zang, C. Wang, ACS Catal. 6 (2016) 6511–6519.
[34] G. Dong, Z. Ai, L. Zhang, Water Res. 66 (2014) 22–30.
[35] K. Balakrishnan, A. Datar, R. Oitker, H. Chen, J. Zuo, L. Zang, J. Am. Chem. Soc. 127 (2005) 10496–10497.
[36] Q. Bao, B.M. Goh, B. Yan, T. Yu, Z. Shen, K.P. Loh, Adv. Mater. 22 (2010) 3661–3666.
[37] Z. Ding, X. Chen, M. Antonietti, X. Wang, ChemSusChem 4 (2011) 274–281.
[38] Z. Qin, J. Zhang, H. Zhou, Y. Song, T. He, Nucl. Instrum. Methods Phys. Res. Sect. 170 (2000) 406–412.
[39] Z. Lin, G. Waller, Y. Liu, M. Liu, C.P. Wong, Adv. Energy Mater. 2 (2012) 884–888.
[40] M.A. Hasan, M.I. Zaki, L. Pasupulety, K. Kumari, Appl. Catal. A Gen. 181 (1999) 171–179.
[41] X. Zhang, B. Peng, S. Zhang, T. Peng, ACS Sustain. Chem. Eng. 3 (2015) 1501–1509.
[42] K. Gelderman, L. Lee, S.W. Donne, J. Chem. Educ. 84 (2007) 685.
[43] J. Ma, C. Wang, H. He, Appl. Catal. B Environ. 184 (2016) 28–34.
[44] Y. Hou, A.B. Laursen, J. Zhang, G. Zhang, Y. Zhu, X. Wang, S. Dahl, I. Chorkendorff, Angew. Chem. Int. Ed. 52 (2013) 3621–3625.